metals

MDPI

Article

Analysis of Nonuniform Deformation in Aluminum Wires Under Varying Torsional Loads Using EBSD Measurement and Multiscale Crystal Plasticity

Mohammad Javad Rezaei [1], Fernando Warchomicka [2], Maria Cecilia Poletti [2,3,*], Mojtaba Pourbashiri [2] and Mohammad Sedighi [1]

[1] School of Mechanical Engineering, Iran University of Science and Technology (IUST), Tehran 1684613114, Iran; mohammd_rezaei@mecheng.iust.ac.ir (M.J.R.); sedighi@iust.ac.ir (M.S.)
[2] Institute of Materials Science, Joining and Forming (IMAT), Graz University of Technology, 8010 Graz, Austria; fernando.warchomicka@tugraz.at (F.W.); mpourbashiri@alumni.iust.ac.ir (M.P.)
[3] Christian Doppler Laboratory for Design of High-Performance Alloys by Thermomechanical Processing, 8010 Graz, Austria
* Correspondence: cecilia.poletti@tugraz.at; Tel.: +43-(316)-873-1676

Abstract: Computational crystal plasticity (CP) models are widely utilized in the literature to analyze the deformation responses of materials at the microstructural level under macroscopic loading conditions. The challenge of connecting changes in texture with macroscopic loading can be effectively addressed through a multiscale CPFE approach. This research focuses on bridging changes in texture and macroscopic loading in pure aluminum wire under torsional loading through the innovative use of the multiscale CP finite element simulation approach and integration with experimental data. The study deals with the effects of the initial average grain size, strain rate, and strains on microstructural evolution at room temperature and mechanical properties. An inhomogeneous initial texture for an as-received specimen was extracted using EBSD measurements and assigned to a CP code to solve the multiscale CPFEM simulations. Changes in texture obtained from pole figures indicated that the A $(11\bar{1})[1\bar{1}0]$, B $(11\bar{2})[1\bar{1}0]$, $\overline{B}$ $(\bar{1}\bar{1}2)[\bar{1}10]$, C $(100)[0\bar{1}1]$, A_1^* $(11\bar{1})[2\bar{1}1]$, and $A_2^*(1\bar{1}1)$ $[\bar{2}\bar{1}1]$ components had the highest frequencies among the torsional tests. The analysis of the resulting texture through the Taylor factor (TF) revealed that the average TF distribution increased from 2.65 to 3.04 when the local strain increased from 0.5 to 2.5 revolutions. Furthermore, an increase in the number of rotations from 0.5 to 2.5 resulted in an 11% increase in average hardness near the outer surface of specimens with an average grain size of 55 μm.

Keywords: multiscale modeling; crystal plasticity simulation; changes in texture

check for updates

Academic Editor: Javier Segurado

Received: 16 December 2024
Revised: 23 January 2025
Accepted: 27 January 2025
Published: 30 January 2025

Citation: Rezaei, M.J.; Warchomicka, F.; Poletti, M.C.; Pourbashiri, M.; Sedighi, M. Analysis of Nonuniform Deformation in Aluminum Wires Under Varying Torsional Loads Using EBSD Measurement and Multiscale Crystal Plasticity. *Metals* **2025**, *15*, 145. https://doi.org/10.3390/met15020145

Copyright: © 2025 by the authors. Licensee MDPI, Basel, Switzerland. This article is an open access article distributed under the terms and conditions of the Creative Commons Attribution (CC BY) license (https://creativecommons.org/licenses/by/4.0/).

1. Introduction

One strategy to enhance materials' mechanical properties involves applying plastic deformation processes [1,2]. The use of plastic deformation methods alters the microstructure of materials, improving their mechanical characteristics, such as strength, ductility, and toughness [3]. Strain hardening or work hardening based on torsion strains has been used in the last several decades to achieve these goals in commercially pure aluminum alloys by increasing dislocation density [4,5]. Additionally, the torsion process has attracted significant interest in plastic deformation techniques due to its capability to generate gradient microstructures [6,7]. Understanding the distribution of shear stress and grain-boundary

rotation in torsional shear deformation is essential for predicting and controlling the mechanical properties and microstructural evolution of materials subjected to this deformation mode [8].

Nonuniform deformation during torsion can lead to variations in strain–stress distribution, grain boundary effects, material anisotropy, surface effects, and nonuniform microstructure evolution within the material [9,10]. These effects are significant in plastic deformation processes such as torsion, drawing, and compression, where the evolution of microstructure is completely reliant on the material's mechanical properties [11–13]. In metallic materials, the Schmid and Taylor factors are used to quantify microstructural evolution and to determine the slip plane and the slip direction of a deformed material [14,15].

The crystal plasticity finite element method (CPFEM) integrates crystal plasticity theory with finite element analysis to facilitate the prediction of material responses at the microstructural level, thereby providing a more comprehensive understanding of deformation mechanisms [16]. The CPFEM approach encompasses the investigation of crystal anisotropy, dislocation dynamics, and grain interactions. In this field of science, Wang et al. conducted a multiscale numerical investigation of deep drawing of aluminum alloy by crystal plasticity and a stress-invariant based anisotropic yield function under the nonassociated flow rule [17]. Prediction of grain refinement using a multiscale, crystal-plasticity-integrated, dislocation-density-based model in multiphase steel alloys was presented by Parmar and Shin [18]. Agius et al. utilized a crystal plasticity model that described grain size effects and slip system interactions on the deformation of austenitic stainless steels [19]. Their proposed model was evaluated at the mesoscale and macroscale based on two-dimensional simulations and three-dimensional modeling. A new crystal plasticity model developed for nanocrystalline metals based on dislocation density evolution and grain boundary interactions was presented by Cappola et al. [20]. Chandra et al. investigated the influence of textural variability on the plastic response of porous crystals embedded in polycrystalline aggregate and the prediction of porosity distribution effects on the orientation-induced plastic anisotropy of ductile solids using the crystal plasticity approach [21,22]. Using the CPFEM approach, the heterogeneity of torsion-created structures can be investigated [23,24]. This approach can also be used to study active slip systems in the alloy during the torsion process [25]. Recently, CPFEM has been combined with artificial intelligence to predict microstructural evolution under various loadings [26–28]. Mao et al. used a deep-learning-based crystal plasticity finite element model to predict mechanical properties [29]. They incorporated an automatic encoder to refine the representation of deformation tensors, which greatly improved the input quality for the ridge regression model. Wang et al. used machine learning methods to identify plastic slips in rate-independent crystal plasticity models [30].

Studying phenomena at various resolution scales, researchers have used multiscale methods widely. Multiscale methods apply both fine-scale and coarse-scale analyses to problems. Integrating information across different scales and considering various deformation mechanisms can predict material behavior more accurately, leading to better material design for specific applications [31]. Therefore, the multiscale methodology requires communication across various material scales [32,33]. The multiscale modeling (FE^2) technique is used to create a connection between the larger-scale model and the smaller-scale model [34–37]. For instance, the behavior of each point at each instant of time on a smaller scale can be investigated with the help of the Düsseldorf Advanced Materials Simulation Kit (DAMASK- Max Planck Institute for Iron Research (Düsseldorf, Germany)) crystal plasticity (CP) code [24,38,39]. The combination of FE^2 and crystal plasticity techniques (called multiscale CP simulation) has been used in microstructural evolution studies. The multiscale methods allow for many length and time scales [40,41] to be incorporated in

solving material/structural analysis problems, reducing the computational costs associated with a traditional refined simulation method. For example, the macroscopic response of full-sized engineering structures can be analyzed based on microscopic processes in crystal plasticity. Lu et al. studied a hierarchical multiscale crystal plasticity model for refractory multi-principal-element alloys [42]. Petkov et al. presented the evaluation of the local stress state caused by grain boundary sliding during creep in the framework of multiscale finite element crystal plasticity [43]. Wu et al. investigated multiscale crystal plasticity finite element method (CPFEM) simulations for shear band development in aluminum alloys [44]. Han et al. studied microstructure-based multiscale modeling of large-strain plastic deformation by coupling a full-field crystal plasticity–spectral solver with an implicit finite element solver [45]. Kohar et al. developed an innovative multiscale framework designed to incorporate microstructural evolution into phenomenological plasticity models [46]. Huang et al. conducted a high-resolution reconstruction-based investigation of multiscale lamellar microstructures by coupled crystal plasticity [47]. Li et al. introduced a technique to use the crystal plasticity approach to investigate the deformation inhomogeneity of network-structured composites during rolling in high-temperature, single-phase areas at both the macro- and microscales [48].

A previous study demonstrated microstructure and texture evolution to identify crystal misorientation using a hierarchical computational technique combined with macro- and microstructural investigations [24]. An algorithm to analyze high- and low-angle grain boundaries was implemented in Python version 3.8.10. Misorientation angle charts could be obtained from this algorithm, significantly reducing computational and experimental costs.

Hence, the combination of macro- and microscale material properties for microstructural investigations using crystal plasticity simulations has been seen frequently in recent years. Despite these investigations, it can be seen that the texture of a mass of crystals after plastic deformation using the effects of a combination of three vital factors, such as average grain size, strain rate, and strains, on the changes in texture and microstructural features has not yet been investigated. For this reason, this study aims to analyze the microstructure, changes in texture, and mechanical characteristics of pure aluminum subjected to torsional deformation at room temperature, with particular emphasis on assessing the effects of strain rate, average grain size, and strain. As shear strain and strain rate were not uniform across the specimen, the localized values of shear strain and stress are reported based on the distance from the center, aligning with the measurement locations for hardness and orientation distribution after the tests. Multiscale modeling techniques and crystal plasticity theory were employed to obtain the change of texture and validated with experimental tests. Microstructural evolutions, including texture and Schmid and Taylor factors, were measured using electron backscattered diffraction (EBSD) and CPFEM analyses. To investigate the mechanical properties of the specimens, some characteristics, such as local hardness and shear yield stress, were evaluated.

2. Materials and Methods

2.1. Experimental Procedures

2.1.1. Material Definition and Experimental Design

Commercial pure aluminum wires (99.50 in wt%–grade 1350) were studied. The initial average sizes of the wire crystals for as-received and annealing specimens were 55 and 150 μm, respectively. Additionally, for the annealed specimen, the thermal conditions of temperature, holding time, and heating rate were 350 °C, 15 min, and 7.7 °C per minute, respectively. The grain size distribution diagram obtained from EBSD measurements, along

with a second-order polynomial fitting curve for the undeformed specimens, is presented in Figure 1.

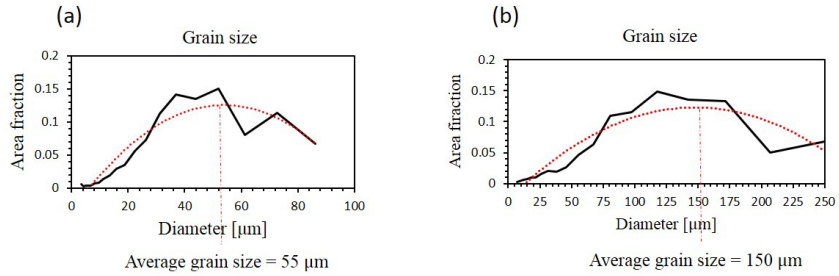

Figure 1. Grain size distribution diagram with second-order polynomial fitting curve (red dotted line) for (**a**) the as-received specimens and (**b**) the annealed specimens.

The as-received and annealed samples consisted of cylinders with diameters of 4 mm, gauge lengths of 30 mm, and total lengths of 90 mm. A length of 30 mm on each side was allocated to fit the grips following the ASTM Test Standard for metallic wires. The torsion tests were carried out according to ASTM-A938-97 [49] at a 0.2 rpm strain rate for extracted the initial mechanical properties. Table 1 summarizes the testing parameters and the initial average grain size, strain rate (twist speed), and strains (revolution).

Table 1. Design of experiment for torsional loading tests.

Test No.	Average Grain Size [μm]	Strain Rate [rpm]	Revolution [Turn]
T1	55	0.5	0.5
T2	150	0.5	0.5
T3	55	5.0	0.5
T4	150	5.0	0.5
T5	55	0.5	2.5
T6	150	0.5	2.5
T7	55	5.0	2.5
T8	150	5.0	2.5

2.1.2. Hardness Measurements

We correlated the hardness values with local strain. Therefore, we measured the micro-Vickers hardness following the procedure shown in Figure 2 (three columns of 9 each), examining the wires in cross-section with the Zwick Roell DuraScan 70 G5 microhardness tester machine (ZwickRoell GmbH & Co. KG, Fürstenfeld, Austria). The applied load and dwell time for hardness investigations were 200 g and 15 s, respectively, based on the ISO 6507/ASTM E384 standards [50,51].

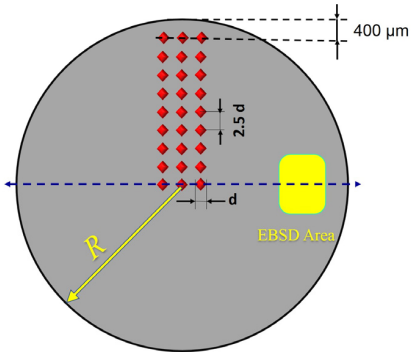

Figure 2. Schematic illustration of the position of hardness measurement on the transverse section of deformed and undeformed specimens. The yellow square shows the area of the EBSD measurement.

2.1.3. Metallography and EBSD Measurements

Microstructural investigations were carried out in the cross-section of the specimens at ~400 µm from the border, representative of the total shear strain (Figure 2). In three states, the as-received condition, after annealing, and after deformation, the specimens were prepared metallographically. Therefore, specimens were embedded and ground with silicon carbide papers up to 2000 grit and then underwent a three-stage polishing process, with a final step using oxide polishing suspension (OP-S).

The aim of the electron backscatter diffraction (EBSD) tests was to obtain the changes in texture given by the pole figure, inverse pole figure, misorientation distribution, Taylor factor (TF), and Schmid factor (SF). For acquisition, a scanning electron microscope field emission gun provided by Tescan (model Mira3) TESCAN GROUP, a.s. Libušina tř. 21623 00 Brno–Kohoutovice Czech Republic) was used with an EBSD Hikari camera (EDAX-AMETEK, Tilburg, The Netherlands) and the software APEX V2.5.1. The measurements covered an area of 400 µm × 800 µm for coarser grains and 300 µm × 600 µm, with a depth of 500 µm, for finer grains, with a step size of 1 µm, an acceleration voltage of 28 kV, a beam intensity of 18, and a working distance between 17 and 20 mm. The number of crystals considered in this fine region for CPFEM simulation was 512. The Taylor factor was obtained from the EBSD measurements and the shear stress state obtained on a transverse cross-section.

2.2. Computational Procedure

The fundamentals of crystal plasticity are categorized within the domain of crystal mechanics studies. This field of mechanics is situated within both dislocation and continuum mechanics theories, utilizing principles from both theories [32,52]. Based on the deformation behavior in CP theory, plastic deformation causes permanent changes in shape without affecting the crystallographic orientation, whereas elastic deformation results in reversible alterations in the crystallographic lattice deformation along with changes in crystallographic orientation.

The constitutive model used in crystal plasticity theory is explained below. The deformation gradient **F** is a fundamental tensor that describes the mapping from a material's initial configuration to its deformed configuration. The deformation gradient **F** can be expressed as $\mathbf{F} = \mathbf{F}^{e}\mathbf{F}^{p}$, where $\mathbf{F}^{e}$ is the elastic deformation gradient and $\mathbf{F}^{p}$ is the plastic deformation gradient [53–55]. The elastic deformation gradient represents the distortion of the crystal lattice that can recover when external forces are removed; it relates to the Cauchy stress tensor through the elastic constitutive laws. This can be written as [55]:

$$\sigma = \mathbf{C}^{e} : \mathbf{E}^{e} \tag{1}$$

where $\mathbf{C}^{e}$ is the elastic stiffness tensor and $\mathbf{E}^{e}$ is the elastic Green–Lagrange strain, derived from $\mathbf{F}^{e}$. By using the flowing equation, the evolution of $\mathbf{F}^{p}$ is expressed in terms of the plastic velocity gradient $\mathbf{L}^{p}$ [55].

$$\dot{\mathbf{F}}^{p} = \mathbf{L}^{p}\mathbf{F}^{p} \tag{2}$$

$\mathbf{L}^{p}$ represents the sum of shear rates for all slip systems [56]:

$$\mathbf{L}^{p} = \sum_{\alpha=1}^{n} \dot{\gamma}^{\alpha}\mathbf{m}^{\alpha} \bigotimes \mathbf{n}^{\alpha} \tag{3}$$

where $\mathbf{m}^{\alpha}$ and $\mathbf{n}^{\alpha}$ are unit vectors describing the slip direction and the normal to the slip plane of the slip system α, respectively, and $\dot{\gamma}^{\alpha}$ is the shear rate on the slip system. The phenomenological constitutive model is widely employed in multiscale simulations to bridge the macroscopic mechanical behavior of materials with the microscale mechanisms,

specifically the deformation and slip processes within crystals [57]. This model relies on critical resolved shear stress (τ_c^{α}) values to determine the activated slip systems under specific loading conditions. The shear rate on slip system α, $\dot{\gamma}^{\alpha}$, is also calculated according to reserved shear stress in every slip system, α, as follows [58]:

$$\dot{\gamma}^{\alpha} = \dot{\gamma}_0 \left| \frac{\tau^{\alpha}}{\tau_c^{\alpha}} \right|^{\frac{1}{m}} \mathrm{sgn}(\tau^{\alpha}) \tag{4}$$

where τ^{α} is the resolved shear stress, τ_c^{α} is the critical resolved shear stress for the slip system α, $\dot{\gamma}_0$ is the reference shear rate, and m is rate sensitivity of slip. The effect of a given set of slip system, β, on the hardening of a specific slip system α can be described as follows:

$$\dot{\tau}_c^{\alpha} = \sum_{\beta=1}^{n} h_{\alpha\beta} \left| \dot{\gamma}^{\beta} \right| \tag{5}$$

where $h_{\alpha\beta}$ is the hardening matrix, defining how much slip system β influences slip system α. The interaction matrix is crucial in multiscale crystal plasticity models because it represents the anisotropy of material hardening and deformation. Using this model, one may forecast a material's macroscopic behavior depending on its microstructure. The hardening matrix can be expressed by:

$$h_{\alpha\beta} = q_{\alpha\beta} \left[h_0 \left(1 - \frac{\tau_c^{\beta}}{\tau_s} \right)^{a} \right] \tag{6}$$

where $q_{\alpha\beta}$ is the latent hardening matrix describing behavior of a crystallite, h_0 is the reference hardening rate of the slip system, τ_c^{β} is the critical shear resistance on the slip system (β), and τ_s is the slip system's shear resistance under saturated conditions. In this study, the plastic deformation of aluminum at room temperature was modeled considering 12 active slip systems. These systems were defined by <110> crystallographic slip directions and {111} slip planes.

The FE² technique, known as a multiscale problem formulation in computational mechanics, provides a framework for systematically bridging for investigation of materials or structures across macroscopic and microscopic scales. In this study, we investigated a twisting process with the help of two submodels. This method is a multiscale approach to address the interactions between micro- and macrolevel mechanisms, which was used for an aluminum wire under torsion process. In the macroscopic (global) model, the material was treated as a homogeneous continuum. In this scale, the constitutive behavior was described by the J2 plasticity model (von Mises yield criterion) with isotropic hardening, and the simulations were carried out using the Abaqus/Explicit solver to capture the bulk deformation responses. The submodel technique in Abaqus was used to connect the macroscopic (global) and microscopic (submodel) models. A combination of the Abaqus/Standard solver and the Düsseldorf Advanced Materials Simulation Kit (DAMASK) software version 2.0.2 was used to simulate the multiscale crystal plasticity of pure commercial aluminum wire under torsional deformation based on the equations in Section 2.2. This method, known as the full-field crystal plasticity finite element method (CPFEM), provides a comprehensive approach to modeling the microstructure behavior of materials [35,59,60]. Both the global model and the submodel used solid elements. As shown in Figure 3, the multiscale system that connected the macroscopic behavior and microscopic mechanics was developed using the equations below.

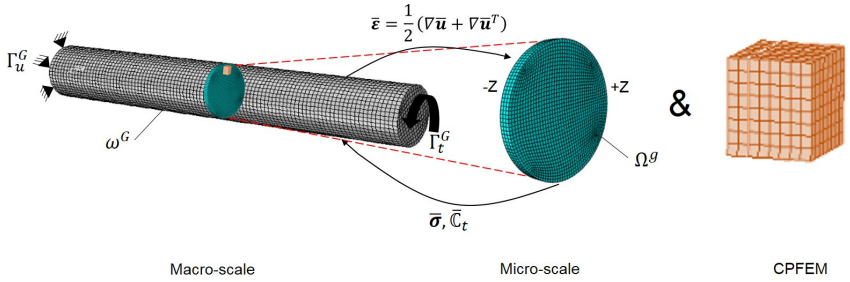

Figure 3. A hierarchical computational framework of the multiscale finite element method (FE^2) for the current problem.

Both scales were addressed through the finite element method utilizing the FE^2 multiscale technique, which facilitates simultaneous computations at both the macro- and microlevels. At the macroscopic scale, the formulations are as follows [61]:

$$\int_{\omega^G} \boldsymbol{\sigma}^G \,:\, \delta\boldsymbol{\varepsilon}^G d\omega^G = \int_{\Gamma_t^G} \boldsymbol{j}^G . \delta\boldsymbol{u}^G d\Gamma_t^G \tag{7}$$

where ω^G is the macroscopic domain, $\boldsymbol{\sigma}^G$ is the macroscopic Cauchy stress tensor, $\delta\boldsymbol{\varepsilon}^G$ is the virtual strain tensor, $\boldsymbol{j}^G$ is the applied tractions on the boundary Γ_t^G (Neumann's condition), and $\delta\boldsymbol{u}^G$ is the virtual displacement. The RVE is shown by the domain Ω^g, and $\bar{\boldsymbol{u}}$ in Figure 4 demonstrates the macroscopic displacement vector.

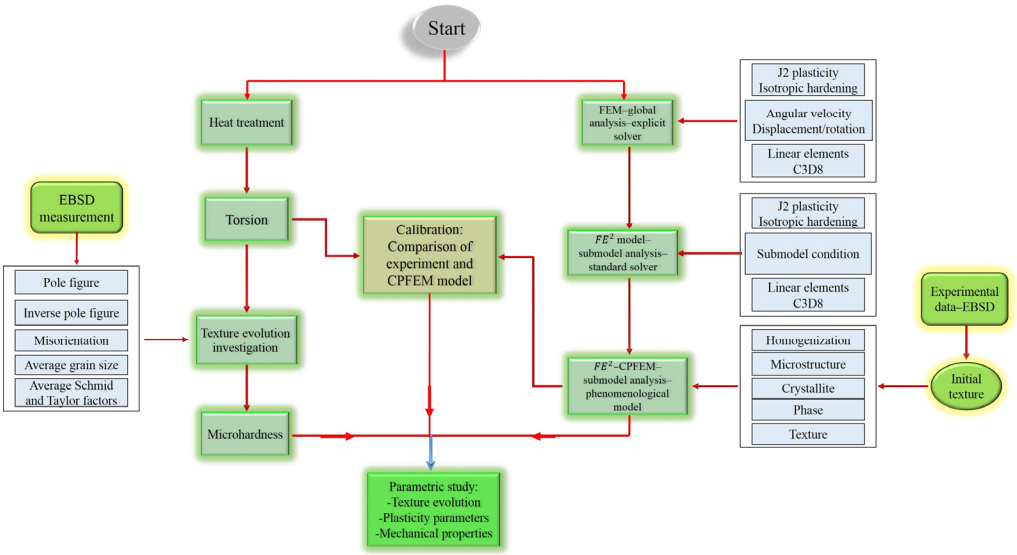

Figure 4. Flow chart used to characterize and model the microstructure evolution and mechanical properties using multiscale CPFEM and EBSD tests.

The microscale problem is typically solved using an RVE. The macroscopic stress $\overline{\sigma}$ and the tangent constitutive matrix $\overline{\mathbb{C}}_t$ for each material point in the RVE are as follows:

$$\overline{\boldsymbol{\sigma}} = \frac{1}{|\Omega^g|}\int_{\Omega^g} \sigma d\Omega^g \tag{8}$$

$$\overline{\mathbb{C}}_t = \frac{\partial\overline{\boldsymbol{\sigma}}}{\partial\overline{\boldsymbol{\varepsilon}}} \tag{9}$$

where Ω^g is the microscopic domain and $\boldsymbol{\sigma}$ is the microscopic stress tensor. The following equation can be computed to determine the remaining microscopic variables:

$$\int_{\Omega^g} \boldsymbol{\sigma} \ : \ \delta\boldsymbol{\varepsilon} d\Omega^g = 0 \tag{10}$$

$$\boldsymbol{\sigma} = \mathbb{C}_t^{(r)} : d\boldsymbol{\varepsilon} \tag{11}$$

$$\overline{\boldsymbol{u}}^g = \overline{\boldsymbol{\varepsilon}}.\left(\boldsymbol{z}^+ - \boldsymbol{z}^-\right) \quad \text{on} \quad \delta\Omega^g \text{ domin} \tag{12}$$

where $\delta\boldsymbol{\varepsilon}$ is the virtual strain tensor at the microscale, $\boldsymbol{\sigma}$ is the microscale stress tensor, the phase r constitutive tensor is given as $\mathbb{C}_t^{(r)}$, $\overline{\boldsymbol{u}}^g$ is the displacement vector at the microscopic domain, $\boldsymbol{z}^{+,-}$ are the coordinates of the microscopic point, and $\overline{\boldsymbol{\varepsilon}}$ is the strain with periodic boundary conditions subjected to applied macroscopic load.

The flow chart of the multiscale CPFEM simulation and experimentally microstructure evolution in this study is shown in Figure 4.

A two-step submodeling technique was applied in a multiscale approach (FE^2). A global model of the aimed process had to be constructed to apply the submodel technique. A total of 18,425 C3D8 elements were used in the global model. This element was an eight-node, three-dimensional hexahedral finite element utilized in Abaqus for simulations. Physical quantities (such as displacements, stresses, and strains) were estimated at the nodes in a finite element model. The submodels were run as separate analyses from the global analysis. The link between the submodels and the global model was the transfer of the time-dependent values of variables saved in the global analysis to the relevant boundary nodes of the submodels. This transfer was accomplished by saving the results from the global model, either in the results file or in the output database, and then reading these results into the submodel analyses. The first step in multiscale modeling was to model the torsion process in three-dimensional models as a global model by using the Abaqus finite element method (FEM) with explicit dynamics solver. Abaqus/Explicit uses an explicit time integration method, avoiding convergence challenges. As the first submodel, the analysis was replicated using the thin disk extracted from the global model by using the Abaqus Standard solver with solid-to-solid elements (global- to submodel). The Abaqus/Standard solver is extensively utilized for multiscale crystal plasticity simulations, as it effectively facilitates macro–micro coupling (e.g., FE^2 methods) and accommodates the iterative computations required to capture the nonlinear characteristics of crystal plasticity, including slip system evolution, grain interactions, and texture formation. The secondary submodel (submodel 2) was generated near the outer surface of the wire and coupled with the crystal plasticity code. The crystal plasticity constitutive model was implemented into the Abaqus/Standard FE by using the DAMASK code. Using crystal plasticity constitutive description rendered the finite element method as an elegant tool for detailed simulation studies of change in texture and strain distribution under realistic boundary conditions. The boundary conditions and loading conditions were periodically retrieved from the global model, and there was no need to define them in each submodel [62]. Gaussian integration points are designated locations within an element where numerical integration occurs. At these points, integrals of various functions, including stress, strain, and other field variables, were computed to determine physical quantities. Step by step, the modeling process is described below in points 1 to 4 based on the above explanation.

(1) Global Model Construction:

First, a global model of the desired process had to be constructed. This model used 18,425 C3D8 elements (eight-node, three-dimensional hexahedral finite elements) that were used in Abaqus for simulations.

(2) Running the Global Model and Transferring Results:

The global model was run as a separate analysis from the submodel analyses. The link between the global model and the submodels involved transferring the time-dependent values of variables saved in the global analysis to the relevant boundary nodes of the submodels. This transfer was accomplished by saving the results from the global model in the results file and then reading these results into the submodel analyses.

(3) Creating the First Submodel (Submodel 1):

The first submodel was created by extracting a thin disk from the global model and using the Abaqus Standard solver with solid-to-solid elements (global- to submodel). Abaqus/Standard is widely used for multiscale crystal plasticity simulations, as it effectively facilitates macro–micro coupling (e.g., FE^2 methods).

(4) Creating the Second Submodel (RVE):

The second submodel was generated near the outer surface of the wire and coupled with a crystal plasticity code. The crystal plasticity constitutive model was implemented into Abaqus/Standard FE using the DAMASK code.

The schematic of geometry and RVE position for multiscale CPFE simulation is illustrated in Figure 5.

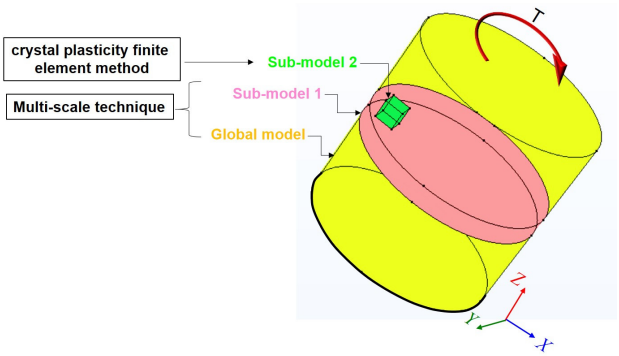

Figure 5. Geometry of multiscale CPFE computational framework of torsional loading.

3. Results and Discussion

3.1. Initial Microstructure and Mechanical Properties

Figure 6 shows the initial microstructure details, including the electroetch microstructure detected by optical microscope (OM), the orientation distribution (color-coded maps), and the pole figures of the as-received and annealed specimens extracted from the EBSD analysis.

Based on the results obtained from the measurements, shown in Figure 6, the average grain sizes for the as-received and annealed wires were 55 and 150 µm, respectively. Furthermore, the [100] fiber component appeared in the wires according to the (111) pole figure results. On the other hand, annealing promoted grain growth, and grains with preferred orientation may have grown preferentially because of their lower stored energy and favorable boundary characteristics. This preferential growth led to a redistribution of the texture, as seen in the annealed pole figure. Since the holding time was not long, there was insufficient time for a complete redistribution of orientations and the elimination of the [100] fiber in the annealed specimen. In addition, the average Taylor factors (TFs) for the mentioned specimens were obtained as 2.7 and 2.65, respectively. These experimental initial microstructures (nonrandom textures) were assigned to the material configuration file in the DAMASK code for CPFEM simulations.

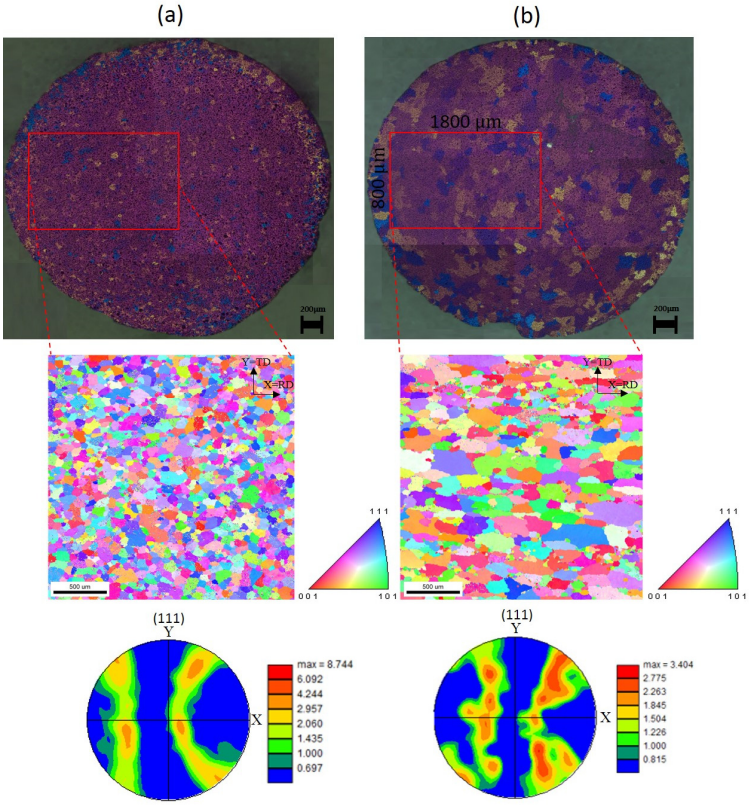

Figure 6. EBSD analysis results and inverse pole and pole figures of the undeformed (**a**) as-received and (**b**) annealed specimens.

The shear stress–strain results, obtained from the experimental torsion test at a strain rate of 0.2 rpm, for the as-received and annealed specimens before torsional deformation are shown in Figure 7. The torque versus angle of twist data obtained from the torsion test were converted into shear stress–shear strain values. It is worth mentioning that the resulting shear stress–shear strain values were calculated at a radius of 2 mm from the center (on the outer surface of the specimen).

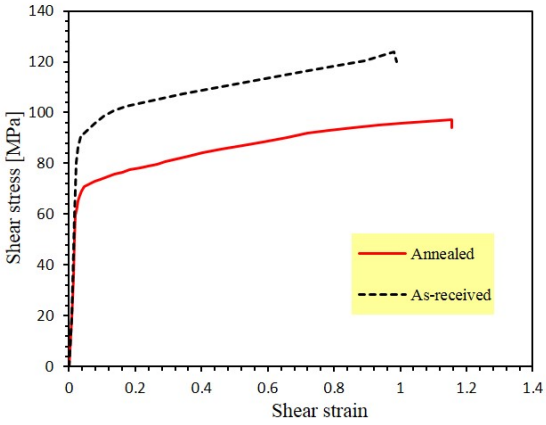

Figure 7. The shear stress–strain curves of pure aluminum under torsion test for as-received and annealed wires.

As shown in Figure 8, the shear yield stresses of the as-received and annealed specimens were 90 and 70 MPa, respectively. Furthermore, the shear strain–stress curve slope of the as-received specimen is higher than that of the annealed specimen. According to this hardening behavior, the maximum shear strengths of the as-received and annealed specimens were obtained as 125 and 90 MPa, respectively.

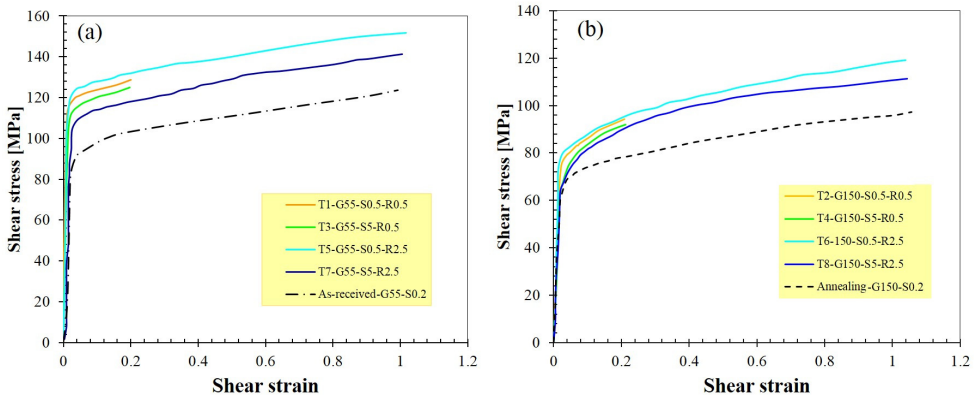

Figure 8. Shear stress–shear strain curves extracted from experimental torsional loading for (**a**) as-received specimens [55 μm] and (**b**) annealing specimens [150 μm].

3.2. Fitting CPFEM Codes and Numerical Analysis with the Experimental Results

Before calibrating the crystal plasticity model, it was essential to evaluate the accuracy of the simulation results in the initial stages of modeling (global model). To verify the validity of the numerical results and avoid presenting mesh convergence, a comparison between the numerical and experimental results was conducted to verify the validity of the numerical results and avoid presenting mesh convergence. For instance, for a rotation of 0.5 revolutions, the numerical shear strain was determined to be 0.2, whereas for a rotation of 2.5 revolutions, it was calculated as 1. For these revolutions, shear strain values of 0.25 and 1.18, respectively, were obtained for submodel 1; the corresponding experimental shear strain values were measured as 0.21 and 1.1, respectively. The close agreement between the numerical and experimental results indicates a high degree of accuracy in the simulations.

The CPFEM model was calibrated using experimental torsion test results and numerical simulations based on the elastic–plastic and hardening behavior of the aluminum rod. The pure torsion process was initially simulated in the Abaqus finite element software using an isotropic hardening model, and the corresponding stress–time curve was extracted. Subsequently, a detailed analysis of the CPFEM was performed, and the stress–time graph was obtained following the CPFEM solution. The stress–time curves from the finite element analysis and the CPFEM solution were iteratively compared, with adjustments made until the CPFEM graph closely matched the finite element simulation graph. This alignment indicated the calibrated parameters in the crystal plasticity model. The stiffness matrix parameters and the calibrated hardening model coefficients obtained through this calibration process are presented in Table 2.

Table 2. Elastic–plastic and hardening model coefficients in CPFEM.

elastic/stiffness matrix	C_{11}[GPa] 104.5		C_{12}[GPa] 53.5		C_{44}[GPa] 26.8
hardening model	τ_s[MPa] 90	τ_0[MPa] 14	h_0[MPa] 109	$\dot{\gamma}_0[s^{-1}]$ 0.02	a 2.25

3.3. Mechanical Properties of Deformed Specimens

3.3.1. Torsion Tests

Figure 8 shows shear stress–shear strain curves for different average grain sizes (G), strain rates (S), and strains (revolutions—R) after the torsion tests.

Figure 8 illustrates the torsional mechanical behavior of the wire specimens, emphasizing the influence of average grain size, strain rate, and strain (rotation) on shear yield stress and overall material performance. In general, by comparing Figure 8a,b, it is evident that

with a decrease in average grain size, the shear yield stress in the as-received specimens was higher than that in the annealed specimens. The influence of strain rate is evident in both figures, with lower strain rates promoting higher shear yield stress because of reduced deformation rates and more uniform strain distribution [63].

Figure 8a shows that reducing the strain rate increased the shear yield stress in specimens with an average grain size of 55 µm. For instance, the shear yield stress of specimen T7 at a strain rate of 5 rpm was 108 MPa. When the strain rate was reduced to 0.5 rpm (specimen T5-G55-S0.5-R2.5), the shear yield stress increased to 124 MPa, representing a 13% improvement. In specimens with 0.5 revolutions (T1 and T3), the shear yield stress increased from 114 MPa in T3 to 120 MPa in T1, showing a 5% enhancement. This improvement occurred as the strain rate was reduced from 5 rpm in T3 to 0.5 rpm in T1. Similarly, in specimens with an average grain size of 150 µm (Figure 8b), reducing the strain rate led to an increase in shear yield stress. For instance, the shear yield stress of T8 (5 rpm) was 70 MPa, which increased to 81 MPa in T6 (0.5 rpm), reflecting a 13.6% enhancement. Furthermore, the shear yield stress increased from 72 MPa in T4 to 79 MPa in T2, representing a 9% improvement.

As the strain rate decreased, the shear yield stress in aluminum increased under torsional loading because of time-dependent plasticity mechanisms, such as dislocation motion and interaction, which become more pronounced at lower strain rates [64]. At lower strain rates, dislocations have more time to move and interact with obstacles. This increased interaction leads to higher dislocation density and entanglement, which increases the resistance to further dislocation motion, raising the yield stress [65,66].

3.3.2. Hardness Tests

Vickers hardness (HV) distributions of as-received and annealing specimens, by different torsional rates and revolutions (based on Table 1) at near the outer surface, are shown in Figure 9. The basis of the measurement was the average maximum hardness value in the defined area. It is necessary to mention that the average initial hardnesses of the annealed and as-received specimens were obtained as 55.8 ± 0.2 and 59 ± 0.2 HV, respectively.

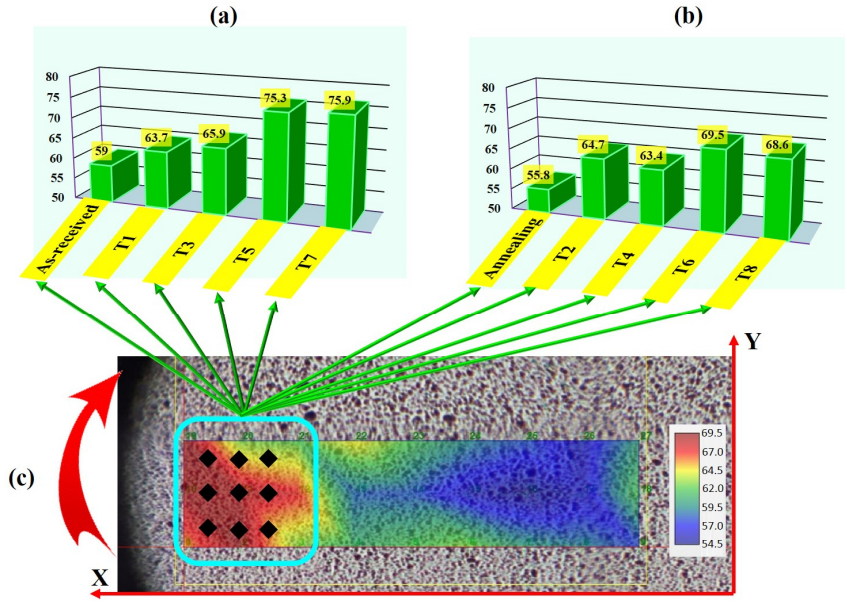

Figure 9. Vickers hardness of as-received and annealed specimens before and after torsional loading: (**a**) as-received wires, (**b**) annealing wires, and (**c**) hardness maps of the measured specimens.

The hardness maps of the measured specimens were similar to what is shown in Figure 9c. The average hardness value (of nine points of measurement) within the light

blue box in Figure 9c for both specimens, as-received and annealed, are presented as line graphs in Figure 9a,b. The hardness of the as-received specimens increased from 59 ± 0.2 HV to 75.9 ± 0.2 HV, while the annealed specimens exhibited an increase in hardness from 55.5 ± 0.2 HV to 69.5 ± 0.2 HV.

The results indicate that increasing the strain (revolutions) from 0.5 to 2.5, as well as increasing the strain rate from 0.5 to 5 rpm, led to a mild increase in the hardness of the wires on the outer surface. According to the graph in Figure 9b, the average hardness of the annealed specimen increased by 8% with an increase in strain rate. Similarly, the average hardness of the as-received specimen increased by 16% as the strain rate increased (Figure 9a). This occurred because of the significant increased in dislocation density as the revolutions increased. Moreover, the findings indicated that smaller average grain size correlated with higher hardness value [65]. In summary, we observe that the hardness increased with increasing strain.

3.4. Microstructural Properties of Deformed Specimens

3.4.1. Texture Development

The experimental pole figures measured by EBSD were compared with selected CPFEM simulation results, as depicted in Figure 10. The pole figure results were obtained on the crystallography plane (111).

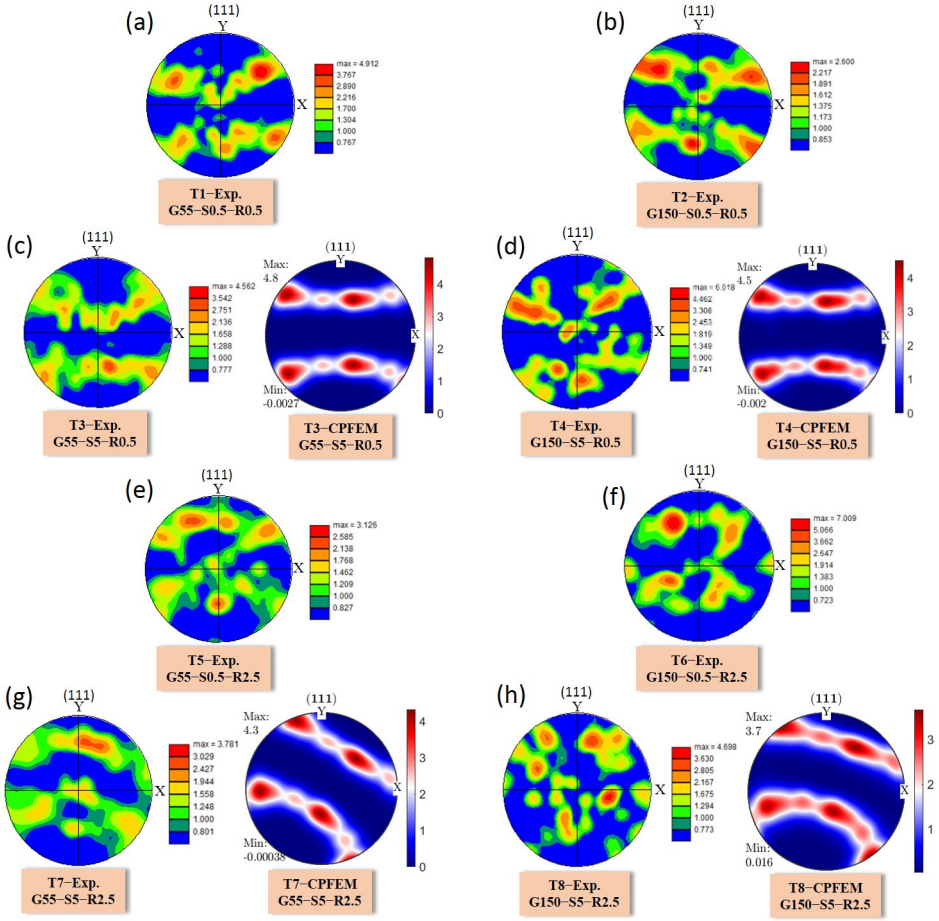

Figure 10. Pole figures of the texture evolution at the plane (111) after deformation. Comparison between experimental EBSD results and simulated CPFEM data: (**a**) T1-experimental, (**b**) T2-experimental, (**c**) T3-experimental and -CPFEM, (**d**) T4-experimental and -CPFEM, (**e**) T5-experimental, (**f**) T6-experimental, (**g**) T7-experimental and -CPFEM, and (**h**) T8-experimental and -CPFEM.

In Figure 10, the density of dots in specific regions of the pole figure indicate the number of grains with specific orientation in the specimen. Furthermore, contour lines are often utilized to depict areas with similar orientation densities, providing a clearer representation of the distribution of grains within the material. The locations of points and contours in various regions of the pole figure signify the active slip systems that appeared during the deformation process. These activated slip systems are called components. The components generated via torsional loading in this study needed to be compared with the ideal components [24] that were formed under pure shear loading. By comparing these components, we could assess how closely the experimentally observed behavior aligned with theoretical or idealized predictions, particularly in terms of slip system activity, grain reorientation, and texture evolution.

It is worth noting that ideal pole figures are required to compare pole figures. In this study, since the loading was pure torsion, the ideal pole figure for pure aluminum under pure torsional loading was used. The texture components formed in both were identified by comparing the pole figures referenced with the simulated pole figure. Although visual differences existed in the annealed samples, there was good agreement in the main texture components of experimental and simulated pole figures. It should be noted that the crystal plasticity model was also calibrated for the annealed samples, in which the initial shear yield stress parameter differed from the previous state.

By comparing the experimental results (EBSD) with the ideal results under torsional loading, it was observed that the $\overline{A}, B, \overline{B}, C, A_1^*$, and A_2^* components appeared in the T1-G55-S0.5-R0.5 test. Additionally, when comparing the T2-G150-S0.5-R0.5 test results with the ideal (111) pole figure, it was revealed that the $A, B, \overline{B}, C, A_1^*$, and A_2^* were created in specimen. In T3-G55-S5-R2.5, by comparing both the EBSD and CPFEM results with the ideal pole figure, it was observed that the $A, B, \overline{B}, C, A_1^*$, and A_2^* components were present in both tests. All components and their corresponding slip systems for both EBSD and CPFEM results are provided in Table 3. These components were compared with the ideal components of pure shear deformation based on the ideal (111) pole figure provided in the reference [24].

Table 3. Comparison of experimental and CPFEM components generated in the T1 to T8 tests with ideal components in pure shear deformation (explanation of the symbols: ● formed, ○ unformed, and - not checked).

		A $(\bar{1}11)$, $[\bar{1}10]$	$\overline{A}$ $(\bar{1}\bar{1}1)$, $[\bar{1}10]$	B $(\bar{1}12)$, $[\bar{1}10]$	$\overline{B}$ $(\bar{1}\bar{1}2)$, $[\bar{1}10]$	C (100), $[0\bar{1}1]$	A_1^* $(\bar{1}11)$, $[\bar{2}11]$	A_2^* $(\bar{1}\bar{1}1)$, $[\bar{2}\bar{1}1]$	Fiber [110]	Fiber <111>
Ideal		●	●	●	●	●	●	●	●	●
T1 (G55-S0.5-R0.5)	**Exp.**	○	●	●	●	●	●	●	-	●
	CPFE	-	-	-	-	-	-	-	-	-
T2 (G150-S0.5-R0.5)	**Exp.**	●	○	●	●	●	●	●	●	●
	CPFE	-	-	-	-	-	-	-	-	-
T3 (G55-S5-R0.5)	**Exp.**	●	○	●	●	●	●	●	●	●
	CPFE	●	○	●	●	●	●	●	●	○
T4 (G150-S5-R0.5)	**Exp.**	○	●	●	●	●	●	○	●	●
	CPFE	○	○	●	●	●	○	●	●	●
T5 (G55-S0.5-R2.5)	**Exp.**	●	●	●	●	●	●	●	●	●
	CPFE	-	-	-	-	-	-	-	-	-
T6 (G150-S0.5-R2.5)	**Exp.**	●	○	●	●	●	●	●	●	●
	CPFE	-	-	-	-	-	-	-	-	-
T7 (G55-S5-R2.5)	**Exp.**	●	○	●	●	●	●	●	●	●
	CPFE	●	●	●	●	●	●	●	○	○
T8 (G150-S5-R2.5)	**Exp.**	●	●	●	●	●	●	●	●	○
	CPFE	●	●	●	○	●	●	●	●	○

It is observed that $A, B, \overline{B}, C, A_1^*$, and A_2^* components had the highest frequency among the mentioned tests. These components in wire specimens arise from the nonuniform distribution of stress and strain within the material as it experiences rotational loading. The different torsional stress responses are caused by different crystal orientations within the wire, activating different slip systems in the specimen.

3.4.2. Taylor Factor (TF) Distribution

The mechanical and anisotropic behavior of metal parts are mainly affected by the orientation effective strength, as measured by the Schmid factor (SF) or Taylor factor (TF). TF is a parameter that can be used to quantify the texture [67,68], and it is a measure to show the amount of plastic work created in the specimen after deformation. This parameter in the present study varied between 2.65 and 3.04. To calculate this parameter based on experimental results (EBSD), it was necessary to define at least five slip systems in the investigated material. The slip systems defined for extracting the TF were (111) $[1\overline{1}0]$, (111) $[01\overline{1}]$, (111) $[10\overline{1}]$, $(\overline{1}11)$ [110], and $(\overline{1}11)$ $[01\overline{1}]$.

The combination of the inverse pole figure (IPF) and TF of the deformed microstructure is illustrated in Figure 11 for CPFEM simulations of tests T3, T4, T7, and T8. These contour bands originated from theoretical calculations based on the Taylor model [69,70], and a specific set of possible active slip systems characterizes them.

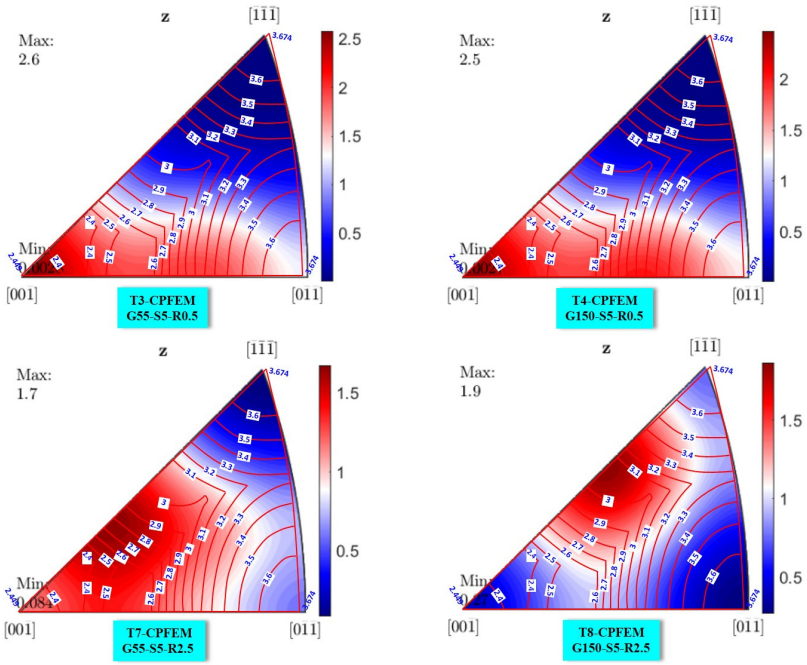

Figure 11. Comparisons between the IPFs of CPFEM and the contour bands of average TF in the direction of the torsion axis.

As shown in Figure 11, the TF was extracted as a function of the orientation of the crystals aligned with the normal direction (Z-axis of the wire). The estimation was derived from the overlap between the colored regions, indicating various misorientations, and the TF contour bands in the standard triangle. The average distribution of TF in CPFEM tests T3 and T7 showed an increase when changing the strain (revolution). The average TF distribution of deformed annealed specimens (T4 and T8) showed similar values for the CPFEM calculations. For both average grain size and constant strain rate, the average distribution of TF changed from 2.7 to 3.0 with standard error of the mean $\pm$ 0.04. The results showed that in tests T4-CPFEM, G150-S5-R0.5, and T8-CPFEM, G150-S5-R2.5, the average distribution of TF approached from 2.65 to 3.1 with standard error of the

mean ± 0.04. In addition, the T7-CPFEM, G55-S5-R2.5, and T8-CPFEM, G150-S5-R2.5, tests clearly showed that the concentration of crystals near the boundary line between [001] and [111] increased with increasing strain rates and strains in torsional loading.

The comparison between the average distributions of TFs obtained from the EBSD measurements and CPFEM simulations is presented in Figure 12.

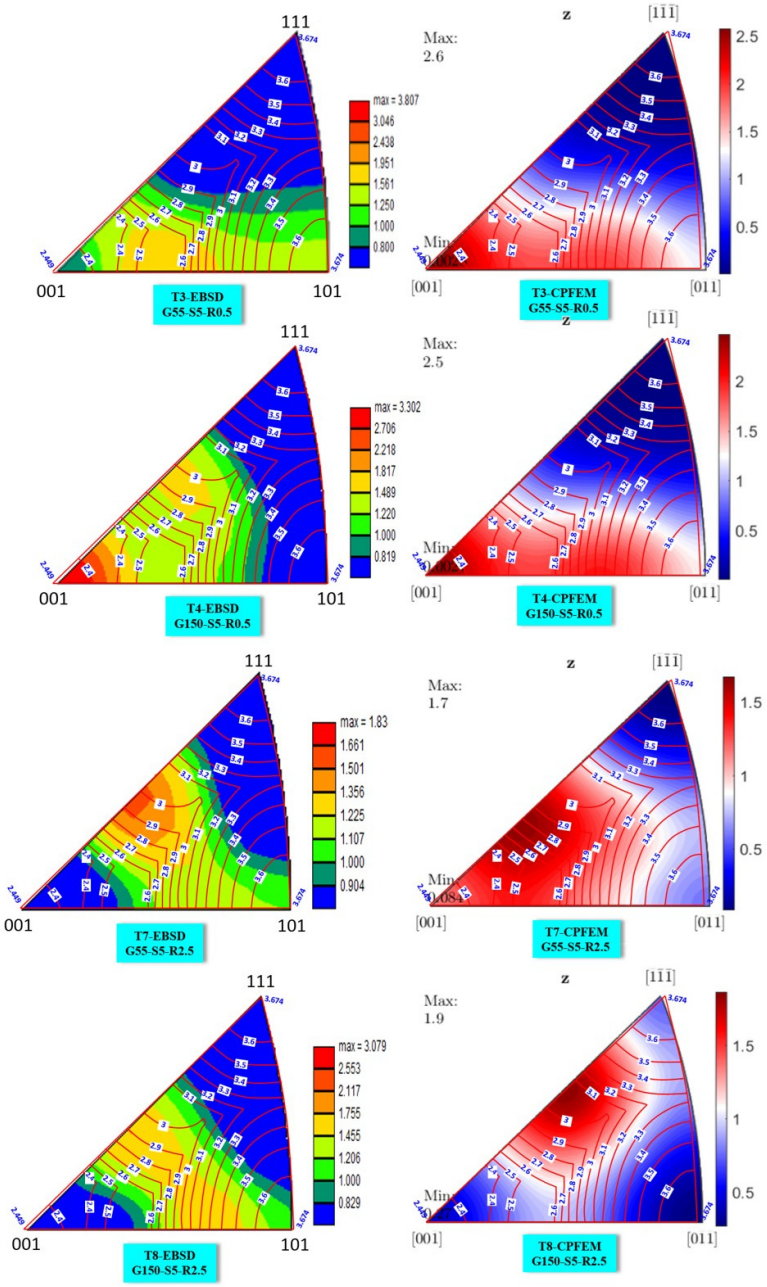

Figure 12. EBSD and CPFEM results of the average distributions of TFs for tests T3, T4, T7, and T8.

The average distribution of TFs of pure aluminum in different torsional loading is demonstrated in Figure 12. It can be seen that as the average grain size and strain increased, the average TF gradually climbed. As both average grain size and strain increased, the material's microstructure changed, leading to more complex interactions between grains. Larger grains in the material structure may have led to the formation of grain boundary effects and substructures, which would have increased the shear stress required for continued plastic deformation. This factor contributed to the rise in the average TF within the material. The comparison between the EBSD and CPFEM results of Test T3 showed that

the average of the experimental TF ranged from approximately 2.7 to 2.8 ± 0.04, which was consistent with the CPFEM specimen in the same range. In contrast, for Test T4, the comparison between the EBSD measurement and CPFEM simulation indicated that the average TF obtained from EBSD was approximately 2.8 to 2.9 ± 0.04, while the CPFEM result showed a range between 2.7 and 2.8. In Test 7, the comparison between the EBSD and CPFEM results showed that the average TF in the experimental data ranged from approximately 2.9 to 3 ± 0.04. Similarly, the CPFEM simulation produced an average TF within the same range, from 2.9 to 3 ± 0.04. In Test 8, the experimental TF was around 3, while the CPFEM solution showed a value of approximately 3.1.

Figure 13 summarizes the effects of average grain size (μm), strain rate (rps), and strain on the average of the experimental TF.

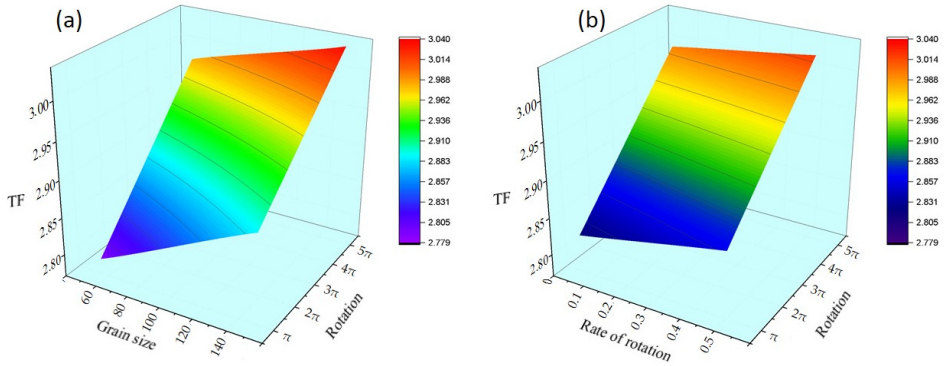

Figure 13. Three-dimensional graph of the impacts of average grain size, strain rate, and strain on average TF during different torsional loadings. (**a**) The average TF based on average grain size and strain; (**b**) the average TF based on strain rate and strain.

It can be seen from Figure 13a that at a constant average grain size of 55 μm, by increasing the number of revolutions, the average TF increased from 2.78 to 3 (an increase of 7.2 percent). Moreover, at the average grain size of 150 μm, the average TF increased gently from 2.83 to 3.04, when the number of revolutions increased from 0.5 to 2.5 (constant strain rate at 5 rpm), indicating a 4.1 percent increase. In Figure 13b, increasing the revolutions had a stronger effect on the average TF than the average grain size. For torsion test at 0.5 rpm, by increasing the revolutions from 0.5 to 2.5, the average TF increased from 2.83 to 2.96 (for a constant average grain size of 55 μm), and for the test at 5 rpm, it increased from 2.86 to 3.03.

The TF indicates a fundamental relationship between microstructural characteristics and the mechanical behavior of materials, particularly in metallic systems during plastic deformation [71]. Based on the results mentioned above, it is observed that with an increase in strain (revolutions) and average grain size, the average TF also rose, leading to the activation of slip systems, strain hardening, and microstructural evolution.

3.4.3. Schmid Factor (SF) Distribution

To explore the effect of the different torsional conditions mentioned in Table 1 on texture evolution, one can use SF distributions calculated from EBSD and CPFEM data. At CPFEM investigation, by using a MATLAB toolbox called MTEX [72], the Schmid factor distributions of specimens from various torsional loadings, taking into account 12 slip systems of the {111} <110> type in FCC material, were calculated and are summarized in Table 4.

Table 4. Schmid factors calculated by CPFEM of the {111} <110> slip systems in FCC aluminum wire.

	Slip System	T3 (G55-S5.0-R0.5)	T4 (G150-S5.0-R0.5)	T7 (G55-S5.0-R2.5)	T8 (G150-S5.0-R2.5)
1	(111) [01$\bar{1}$]	0.4286	0.4286	0.4286	0.4286
2	(111) [$\bar{1}$01]	0.3571	0.3571	0.3571	0.3571
3	(111) [1$\bar{1}$0]	0.4286	0.4286	0.4286	0.4286
4	($\bar{1}\bar{1}$1) [0$\bar{1}\bar{1}$]	0	0	0	0
5	($\bar{1}\bar{1}$1) [101]	0	0	0	0
6	($\bar{1}\bar{1}$1) [$\bar{1}$10]	0	0	0	0
7	(1$\bar{1}\bar{1}$) [0$\bar{1}$1]	0.2857	0.2857	0.2857	0.2857
8	(1$\bar{1}\bar{1}$) [$\bar{1}$0$\bar{1}$]	0.4820	0.4820	0.4820	0.4820
9	(1$\bar{1}\bar{1}$) [110]	0.3571	0.3571	0.3571	0.3571
10	($\bar{1}\bar{1}$1) [011]	0.2143	0.2143	0.2143	0.2143
11	($\bar{1}\bar{1}$1) [10$\bar{1}$]	0.2857	0.2857	0.2857	0.2857
12	($\bar{1}\bar{1}$1) [$\bar{1}\bar{1}$0]	0.4286	0.4286	0.4286	0.4286

As shown in Table 4, the effective slip systems among the {111} <110> type of slip systems in FCC materials in T3-G55-S5-R0.5, T4-G150-S5-R0.5, T7-G55-S5-R2.5, and T8-G150-S5-R2.5 were (111) [01$\bar{1}$], (111) [1$\bar{1}$0], (1$\bar{1}\bar{1}$) [$\bar{1}$0$\bar{1}$], and ($\bar{1}\bar{1}$1) [$\bar{1}\bar{1}$0], with SF values of 0.4286, 0.4286, 0.4820, and 0.4286, respectively. When a material experiences torsional loading, the orientation of the crystals has a major influence on the activation of slip systems. When a crystal's orientation aligns more favorably with the direction of torsion, it has a higher SF, meaning the slip system associated with that orientation is more likely to activate. In torsional loading, the stress distribution is nonuniform, meaning that different parts of the crystal structure experience different forces. This anisotropy in the crystal structure causes varying SFs to appear, leading to heterogeneous activation of slip systems [73,74]. Because of the rotation crystals around the normal direction (Z-axis), the angles of the crystal coordinate system were correlated to the specimen coordinate system, and the SFs were the same in T3-G55-S5-R0.5, T4-G150-S5-R0.5, T7-G55-S5-R2.5, and T8-G150-S5-R2.5, although the parameters in the four tests were different.

The 3D chart in Figure 14 illustrates the distribution of SFs and the average SF value for the crystals obtained through EBSD analysis for the designed tests (T1 to T8).

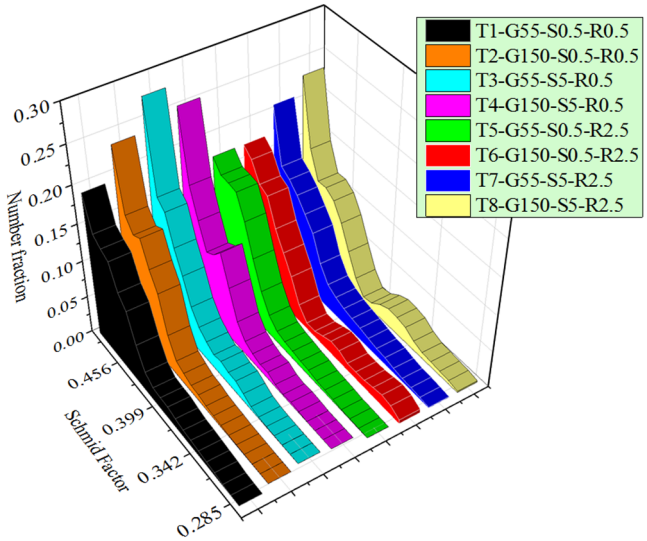

Figure 14. Experimental Schmid factor distribution for tests T1–T8 under torsional loading.

According to the SF distribution on the 3D graph in Figure 14, a large fraction of crystals with slip systems of the {111} <110> type favored activating slipping during torsion

along the normal direction. As is clear from the results presented in Figure 14, T6 and T8-G150-S0.5-R5π had the highest average SF values at 0.4710 and 0.4725, respectively. The increase in SF indicates the facility of slipping of crystal plates as a result of the increase in plastic flow, which means less stress is required for plastic deformation [9]. Annealed specimens had higher SFs than the as-received specimens. The removal of obstacles to dislocation movement due to the heat treatment in specimens T2-G150-S0.5-R0.5, T4-G150-S5-R0.5, T6-G150-S0.5-R2.5, and T8-G150-S5-R2.5 was the reason for this increase. Therefore, more plastic deformation occurred in the material with lower stress.

A 3D surface graph of revolutions' and strain rate factors' effects on the SF is presented in Figure 15 after CPFEM simulation of the torsion tests.

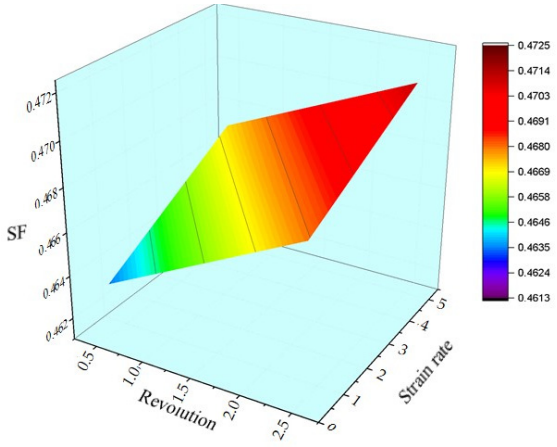

Figure 15. Simulated average of SF as a function of the torsion test for specimens with 55 μm average grain size.

The maximum average SF in the torsional loading on aluminum wires occurred when the strain and strain rate had the highest values. The effect of the increase in strain (revolutions) was greater than that of the increase in the strain rate. Therefore, in a specimen with an average grain size of 55 μm and constant strain rate 0.5 rpm, with an increase in revolutions from 0.5 to 2.5, the average SF increased from 0.4613 to 0.4657, while with an increase in strain rate from 0.5 rpm to 5 rpm, the average SF increased from 0.4657 to 0.4695 in a specimen with an average grain size of 55 μm undergoing a constant 2.5 revolutions. It was concluded that the average SF in wires under torsional loading was more strain-rate dependent than strain dependent. A higher average SF shows that a particular slip system experiences a greater resolved shear stress, thus increasing its activation probability during deformation. In contrast, lower average SFs may have less favorably oriented grains, resulting in delayed slip system activation and enhancing the strain-hardening effect.

4. Conclusions

In this research, the effect of torsional loading at the macroscale on the microstructure evolution and mechanical properties of commercially pure aluminum wires was investigated computationally and experimentally. For this purpose, the effects of average grain size, strain, and strain rate on microstructure evolution during a pure torsion process were compared using EBSD experimental tests and the multiscale crystal plasticity (CPFEM) technique. These comparisons showed that CPFEM could reliably predict the microstructure parameters, change in texture, and orientation distributions during deformation. One of the most notable achievements was that the sensitivity of pure commercial aluminum wires to strain rate and average grain size was confirmed. The results were obtained as follows.

- Experimental investigations with EBSD tests showed that the specimens had a non-random texture (fiber [100]) before torsional loading, and the CPFEM investigations were processed accordingly.
- In wires with an average grain size of 55 μm, the hardness on the external surface after the torsion process increased by 22.3%, and in wires with an average grain size of 150 μm, it increased by 19.7%.
- The most active slip systems during the torsional loading process among the designed tests (T1–T8) were: $(11\bar{1})[1\bar{1}0]$, $(11\bar{2})[1\bar{1}0]$, $(\bar{1}\bar{1}2)[\bar{1}10]$, $(100)[0\bar{1}1]$, $(11\bar{1})[2\bar{1}1]$, and $(1\bar{1}1)[\bar{2}\bar{1}1]$.
- The results showed that in specimens with an average grain size of 55 μm, with an increase in the strain rate from 0.5 to 5 (rpm), the average TF and average SF increased by 10% and 2.5%, respectively, when the strain (revolutions) climbed from 0.5 to 2.5.
- In specimens with an average grain size of 150 μm, with an increase in the strain rate from 0.5 to 5 (rpm), the average TF and average SF increased by 13% and 4%, respectively, when the strain (revolutions) climbed from 0.5 to 2.5.
- For specimens undergoing 0.5 revolutions, increasing the average grain size from 55 to 150 μm at the strain rate of 0.5 rpm caused a 2.8% increase in the average TF, while at the strain rate of 5 rpm, a 4.1% increase in average TF was observed with increasing average grain size.
- For specimens undergoing 2.5 revolutions, at the strain rate of 0.5 rpm, with increasing average grain size, a 2.3% increase in the average TF was observed, while at the strain rate of 5 rpm, only a 1.3% increase occurred.

Author Contributions: Conceptualization, M.J.R. and M.S.; methodology, M.J.R., M.S., M.C.P. and M.P.; software, M.J.R. and M.P.; validation, M.J.R.; formal analysis M.J.R.; investigation, M.J.R.; resources, M.J.R. and M.P.; data curation, M.J.R. and M.S.; writing—original draft preparation, M.J.R.; writing—review and editing, M.S., M.C.P. and F.W.; supervision, M.S., M.C.P. and F.W.; project administration, M.S., M.C.P. and M.P.; funding acquisition, M.C.P. All authors have read and agreed to the published version of the manuscript.

Funding: Parts of this work were funded by the CD-Laboratory for Design of High-Performance Alloys by Thermomechanical Processing and the Christian Doppler Society. The open-access fees were supported by the TU Graz Open Access Publishing Fund.

Data Availability Statement: The raw data supporting the conclusions of this article will be made available by the authors on request.

Acknowledgments: Open Access Funding by the Graz University of Technology.

Conflicts of Interest: The authors declare no conflicts of interest.

References

1. Volokitina, I.; Volokitin, A.; Panin, E.; Fedorova, T.; Lawrinuk, D.; Kolesnikov, A.; Yerzhanov, A.; Gelmanova, Z.; Liseitsev, Y. Improvement of strength and performance properties of copper wire during severe plastic deformation and drawing process. *Case Stud. Constr. Mater.* **2023**, *19*, e02609. [CrossRef]
2. Yin, F.; Ma, S.; Hu, S.; Liu, Y.; Hua, L.; Cheng, G.J. Understanding the microstructure evolution and mechanical behavior of titanium alloy during electrically assisted plastic deformation process. *Mater. Sci. Eng. A* **2023**, *869*, 144815. [CrossRef]
3. Wang, J.; Zhang, D.; Li, Y.; Xiao, Z.; Fouse, J.; Yang, X. Effect of initial orientation on the microstructure and mechanical properties of textured AZ31 Mg alloy during torsion and annealing. *Mater. Des.* **2015**, *86*, 526–535. [CrossRef]
4. Shao, C.W.; Zhang, P.; Zhu, Y.K.; Zhang, Z.J.; Tian, Y.Z.; Zhang, Z.F. Simultaneous improvement of strength and plasticity: Additional work-hardening from gradient microstructure. *Acta Mater.* **2018**, *145*, 413–428. [CrossRef]
5. Pourbashiri, M.; Poletti, C.; Sedighi, M.; Sommitsch, C. Strengthening mechanisms of Al wires processed by equal channel angular torsion drawing. *Mater. Sci. Technol.* **2020**, *36*, 65–82. [CrossRef]

6. Yang, L.; Chen, Z.; Ma, X.; Zhong, D.; Zhao, X.; Xiao, L.; Fang, X. Improvement of strength and ductility in a gradient structured Ni fabricated by severe torsion deformation. *Mater. Sci. Eng. A* **2021**, *826*, 141980. [CrossRef]
7. Liu, Y.; He, Y.; Cai, S. Effect of gradient microstructure on the strength and ductility of medium-entropy alloy processed by severe torsion deformation. *Mater. Sci. Eng. A* **2021**, *801*, 140429. [CrossRef]
8. Li, X.; Lu, L.; Li, J.; Zhang, X.; Gao, H. Mechanical properties and deformation mechanisms of gradient nanostructured metals and alloys. *Nat. Rev. Mater.* **2020**, *5*, 706–723. [CrossRef]
9. Howeyze, M.; Eivani, A.R.; Arabi, H.; Jafarian, H.R. Effects of deformation routes on the evolution of microstructure, texture and tensile properties of AA5052 aluminum alloy. *Mater. Sci. Eng. A* **2018**, *732*, 120–128. [CrossRef]
10. Ziemian, C.W.; McClintock, M.S.; Ziemian, R.D. Experimental investigation of torsional strengths of aluminum alloys: Circular and rectangular solid sections. *Structures* **2024**, *59*, 105776. [CrossRef]
11. Wu, H.; Huang, T.; Song, K.; Li, S.; Zhou, Y.; Zhang, Y. Effect of drawing speed on the deformation characteristics, microstructure and properties of copper wire rod. *Mater. Sci. Eng. A* **2024**, *892*, 146025. [CrossRef]
12. Khamsuk, S.; Park, N.; Gao, S.; Terada, D.; Adachi, H.; Tsuji, N. Mechanical properties of bulk ultrafine grained aluminum fabricated by torsion deformation at various temperatures and strain rates. *Mater. Trans.* **2014**, *55*, 106–113. [CrossRef]
13. Omranpour, B.; Ivanisenko, Y.; Kulagin, R.; Kommel, L.; Sanchez, E.G.; Nugmanov, D.; Scherer, T.; Heczel, A.; Gubicza, J. Evolution of microstructure and hardness in aluminum processed by High Pressure Torsion Extrusion. *Mater. Sci. Eng. A* **2019**, *762*, 138074. [CrossRef]
14. Qiu, R.; Shoja, S.; von Fieandt, L.; Engqvist, J.; Bäcke, O.; Andrén, H.-O.; Halvarsson, M. Schmid factor analysis for chip flow induced plastic deformation of textured cubic carbonitride coatings. *Int. J. Refract. Met. Hard Mater.* **2022**, *108*, 105932. [CrossRef]
15. Rakshit, R.; Sarkar, A.; Panda, S.K.; Mandal, S. Influence of out-of-plane stretch forming induced different strain paths on micro-texture evolution, slip system activity and Taylor factor distribution in Al–Li alloy. *Mater. Sci. Eng. A* **2022**, *830*, 142267. [CrossRef]
16. Azhari, F.; Wallbrink, C.; Sterjovski, Z.; Crawford, B.R.; Menzel, A.; Agius, D.; Wang, C.H.; Schaffer, G. Predicting the complete tensile properties of additively manufactured Ti-6Al-4V by integrating three-dimensional microstructure statistics with a crystal plasticity model. *Int. J. Plast.* **2022**, *148*, 103127. [CrossRef]
17. Wang, S.; Shang, H.; Zhang, Z.; Lou, Y. Multi-scale numerical investigation of deep drawing of 6K21 aluminum alloy by crystal plasticity and a stress-invariant based anisotropic yield function under non-associated flow rule. *J. Manuf. Process.* **2023**, *102*, 736–755. [CrossRef]
18. Parmar, A.; Shin, Y.C. Prediction of grain refinement using multiscale crystal plasticity-integrated dislocation density-based model in multiphase steel alloys. *Comput. Mater. Sci.* **2024**, *242*, 113026. [CrossRef]
19. Agius, D.; Kareer, A.; Al Mamun, A.; Truman, C.; Collins, D.M.; Mostafavi, M.; Knowles, D. A crystal plasticity model that accounts for grain size effects and slip system interactions on the deformation of austenitic stainless steels. *Int. J. Plast.* **2022**, *152*, 103249. [CrossRef]
20. Cappola, J.; Wang, J.; Li, L. A dislocation-density-based crystal plasticity model for FCC nanocrystalline metals incorporating thermally-activated depinning from grain boundaries. *Int. J. Plast.* **2024**, *172*, 103863. [CrossRef]
21. Chandra, S.; Kumar, S.; Samal, M.K.; Chavan, V.M. Influence of textural variability on plastic response of porous crystal embedded in polycrystalline aggregate: A crystal plasticity study. *Int. J. Plast.* **2024**, *182*, 104117. [CrossRef]
22. Chandra, S.; Kumar, S.; Samal, M.K.; Chavan, V.M. Predicting porosity distribution effects on the orientation induced plastic anisotropy of ductile solids: A crystal plasticity investigation. *Int. J. Plast.* **2023**, *171*, 103781. [CrossRef]
23. Tang, X.F.; Peng, L.F.; Shi, S.Q.; Fu, M.W. Influence of crystal structure on size dependent deformation behavior and strain heterogeneity in micro-scale deformation. *Int. J. Plast.* **2019**, *118*, 147–172. [CrossRef]
24. Rezaei, M.J.; Sedighi, M.; Pourbashiri, M. Developing a new method to represent the low and high angle grain boundaries by using multi-scale modeling of crystal plasticity. *J. Alloys Compd.* **2023**, *939*, 168844. [CrossRef]
25. Zoller, K.; Gruber, P.; Ziemann, M.; Görtz, A.; Gumbsch, P.; Schulz, K. Classification of slip system interaction in microwires under torsion. *Comput. Mater. Sci.* **2023**, *216*, 111839. [CrossRef]
26. Zhao, Y.; Xiang, Y.; Tang, K. Machine learning-based fatigue life prediction of lamellar titanium alloys: A microstructural perspective. *Eng. Fract. Mech.* **2024**, *303*, 110106. [CrossRef]
27. Yang, F.; Zhao, W.; Ru, Y.; Pei, Y.; Li, S.; Gong, S.; Xu, H. Predicting the oxidation kinetic rate and near-surface microstructural evolution of alumina-forming Ni-based single crystal superalloy based on machine learning. *Acta Mater.* **2024**, *266*, 119703. [CrossRef]
28. Zhang, Z.; Li, Z.; Tang, S.; Ma, Y.; Liu, W. Predicting the in-plane mechanical anisotropy of 7085 aluminum alloys through crystal plasticity simulations and machine learning. *Mater. Today Commun.* **2024**, *38*, 108381. [CrossRef]
29. Mao, Y.; Keshavarz, S.; Kilic, M.N.T.; Wang, K.; Li, Y.; Reid, A.C.E.; Liao, W.; Choudhary, A.; Agrawal, A. A deep learning-based crystal plasticity finite element model. *Scr. Mater.* **2025**, *254*, 116315. [CrossRef]

30. Wang, Z.; Chen, X.; Wen, J.; Wei, Y. Determining plastic slips in rate-independent crystal plasticity models through machine learning algorithms. *Extrem. Mech. Lett.* **2024**, *71*, 102216. [CrossRef]
31. Yu, P.; Huang, H.; He, S.; Ren, Z. A multiscale methods for prediction of the elastic properties of portland cement blended with fly ash based on X-CT and hydration model. *J. Build. Eng.* **2024**, *89*, 109179. [CrossRef]
32. Long, X.; Chong, K.; Su, Y.; Du, L.; Zhang, G. Connecting the macroscopic and mesoscopic properties of sintered silver nanoparticles by crystal plasticity finite element method. *Eng. Fract. Mech.* **2023**, *281*, 109137. [CrossRef]
33. Shao-lei, L.; Yan-liang, Y.; Qin, G.; Xiao, L.; Ming-hui, S.; Yi-long, L. A novel model to predict microvoid evolution in tensile necking using macroscopic deformation behavior. *J. Mater. Res. Technol.* **2023**, *25*, 2040–2048. [CrossRef]
34. Liu, Z.L.; Liu, X.M.; Zhuang, Z.; You, X.C. A multi-scale computational model of crystal plasticity at submicron-to-nanometer scales. *Int. J. Plast.* **2009**, *25*, 1436–1455. [CrossRef]
35. Raschi, M.; Lloberas-Valls, O.; Huespe, A.; Oliver, J. High performance reduction technique for multiscale finite element modeling (HPR-FE2): Towards industrial multiscale FE software. *Comput. Methods Appl. Mech. Eng.* **2021**, *375*, 113580. [CrossRef]
36. Lu, X.; Yvonnet, J.; Papadopoulos, L.; Kalogeris, I.; Papadopoulos, V. A stochastic FE2 data-driven method for nonlinear multiscale modeling. *Materials* **2021**, *14*, 2875. [CrossRef]
37. Peng, Y.; Zhao, H.; Ye, J.; Yuan, M.; Tian, L.; Li, Z.; Liu, Y. 3D multiscale tri-level finite element analysis of aluminum matrix composites with Nano&Micro hybrid inclusions. *Compos. Struct.* **2023**, *305*, 116545. [CrossRef]
38. Long, X.; Chong, K.; Su, Y.; Chang, C.; Zhao, L. Meso-scale low-cycle fatigue damage of polycrystalline nickel-based alloy by crystal plasticity finite element method. *Int. J. Fatigue* **2023**, *175*, 107778. [CrossRef]
39. Roters, F.; Diehl, M.; Shanthraj, P.; Eisenlohr, P.; Reuber, C.; Wong, S.L.; Maiti, T.; Ebrahimi, A.; Hochrainer, T.; Fabritius, H.-O. DAMASK–The Düsseldorf Advanced Material Simulation Kit for modeling multi-physics crystal plasticity, thermal, and damage phenomena from the single crystal up to the component scale. *Comput. Mater. Sci.* **2019**, *158*, 420–478. [CrossRef]
40. Qin, R.; Zhang, Z.; Huang, J.; Wang, J.; Du, Z.; Wen, G.; He, W. Surface stress monitoring of laser shock peening using AE time-scale texture image and multi-scale blueprint separable convolutional networks with attention mechanism. *Expert Syst. Appl.* **2023**, *224*, 120018. [CrossRef]
41. Li, Y.-H.; Shen, F.; Güler, M.A.; Ke, L.-L. Modeling multi-physics electrical contact on rough surfaces considering elastic-plastic deformation. *Int. J. Mech. Sci.* **2024**, *269*, 109066. [CrossRef]
42. Lu, W.; Chen, Y.; Zhang, W.; Tan, F.; Li, J.; Liu, B.; Liaw, P.K.; Fang, Q. A hierarchical multiscale crystal plasticity model for refractory multi-principal element alloys. *Int. J. Mech. Sci.* **2024**, *271*, 109140. [CrossRef]
43. Petkov, M.P.; Elmukashfi, E.; Tarleton, E.; Cocks, A.C.F. Evaluation of local stress state due to grain-boundary sliding during creep within a crystal plasticity finite element multi-scale framework. *Int. J. Mech. Sci.* **2021**, *211*, 106715. [CrossRef]
44. Wu, Y.; Shen, Y.; Chen, K.; Yu, Y.; He, G.; Wu, P. Multi-scale crystal plasticity finite element method (CPFEM) simulations for shear band development in aluminum alloys. *J. Alloys Compd.* **2017**, *711*, 495–505. [CrossRef]
45. Han, F.; Roters, F.; Raabe, D. Microstructure-based multiscale modeling of large strain plastic deformation by coupling a full-field crystal plasticity-spectral solver with an implicit finite element solver. *Int. J. Plast.* **2020**, *125*, 97–117. [CrossRef]
46. Kohar, C.P.; Bassani, J.L.; Brahme, A.; Muhammad, W.; Mishra, R.K.; Inal, K. A new multi-scale framework to incorporate microstructure evolution in phenomenological plasticity: Theory, explicit finite element formulation, implementation and validation. *Int. J. Plast.* **2019**, *117*, 122–156. [CrossRef]
47. Huang, X.; Chen, Y.; Wang, J.; Lu, G.; Wang, W.; Yao, Z.; Zhao, S.; Liu, Y.; Li, Q. High-resolution reconstruction-based investigation of multi-scale lamellar microstructures by coupled crystal plasticity and in-situ experiment. *Scr. Mater.* **2024**, *241*, 115896. [CrossRef]
48. Li, Z.; Kang, Q.; Xu, X.; Wang, C.; Luo, S.; Wang, G. Multiscale crystal plasticity finite element simulations of the deformation inhomogeneity of TiBw/TA15 composites with network-structured during hot rolling. *J. Mater. Res. Technol.* **2023**, *25*, 183–199. [CrossRef]
49. ASTM International. Standard Test Method for Torsion Testing of Wire. In *The Annual Book of ASTM Standards*; ASTM International: West Conshohocken, PA, USA, 2002; Volume 60, pp. 19–20.
50. *ASTM E384-09*; Standard Test Method for Microindentation Hardness of Materials. ASTM International: West Conshohocken, PA, USA, 1999.
51. Petrík, J.; Blaško, P.; Markulík, Š.; Šolc, M.; Palfy, P. The indentation size effect (ISE) of metals. *Crystals* **2022**, *12*, 795. [CrossRef]
52. He, J.-C.; Zhu, S.-P.; Gao, J.-W.; Liu, R.; Li, W.; Liu, Q.; He, Y.; Wang, Q. Microstructural size effect on the notch fatigue behavior of a Ni-based superalloy using crystal plasticity modelling approach. *Int. J. Plast.* **2024**, *172*, 103857. [CrossRef]
53. Liu, C.; Roters, F.; Raabe, D. Finite strain crystal plasticity-phase field modeling of twin, dislocation, and grain boundary interaction in hexagonal materials. *Acta Mater.* **2023**, *242*, 118444. [CrossRef]
54. Zeng, X.; Liu, C.; Zhao, C.; Dong, J.; Roters, F.; Guan, D. Three-dimensional study of grain scale tensile twinning activity in magnesium: A combination of microstructure characterization and mechanical modeling. *Acta Mater.* **2023**, *255*, 119043. [CrossRef]

55. Roters, F.; Eisenlohr, P.; Hantcherli, L.; Tjahjanto, D.D.; Bieler, T.R.; Raabe, D. Overview of constitutive laws, kinematics, homogenization and multiscale methods in crystal plasticity finite-element modeling: Theory, experiments, applications. *Acta Mater.* **2010**, *58*, 1152–1211. [CrossRef]
56. Lin, P.; Nie, J.; Liu, M. Multiscale crystal plasticity finite element model for investigating the irradiation hardening and defect evolution mechanism of A508-3 steel. *Nucl. Mater. Energy* **2022**, *32*, 101214. [CrossRef]
57. Wang, M.; Wang, X.; Sun, P.; Li, H.; Liu, Z.; Yang, G.; Liu, Y. Multi-scale investigation on grain size effect of a powder metallurgy Ni-based superalloy based on simulation and experimental characterization. *Intermetallics* **2024**, *173*, 108429. [CrossRef]
58. Zhang, K.; Holmedal, B.; Hopperstad, O.S.; Dumoulin, S.; Gawad, J.; Van Bael, A.; Van Bael, A.; Van Houtte, P. Multi-level modelling of mechanical anisotropy of commercial pure aluminium plate: Crystal plasticity models, advanced yield functions and parameter identification. *Int. J. Plast.* **2015**, *66*, 3–30. [CrossRef]
59. Tong, X.; Li, Y.; Fu, M.W. Modelling of grain size effects in progressive microforming using CPFEM. *Int. J. Mech. Sci.* **2024**, *267*, 108971. [CrossRef]
60. Depriester, D.; Goulmy, J.P.; Barrallier, L. Crystal Plasticity simulations of in situ tensile tests: A two-step inverse method for identification of CP parameters, and assessment of CPFEM capabilities. *Int. J. Plast.* **2023**, *168*, 103695. [CrossRef]
61. Su, T.H.; Huang, S.J.; Jean, J.G.; Chen, C.S. Multiscale computational solid mechanics: Data and machine learning. *J. Mech.* **2022**, *38*, 568–585. [CrossRef]
62. Tian, W.; Qi, L.; Chao, X.; Liang, J.; Fu, M. Periodic boundary condition and its numerical implementation algorithm for the evaluation of effective mechanical properties of the composites with complicated micro-structures. *Compos. Part B Eng.* **2019**, *162*, 1–10. [CrossRef]
63. Wang, B.B.; Xie, G.M.; Wu, L.H.; Xue, P.; Ni, D.R.; Xiao, B.L.; Liu, Y.D.; Ma, Z.Y. Grain size effect on tensile deformation behaviors of pure aluminum. *Mater. Sci. Eng. A* **2021**, *820*, 141504. [CrossRef]
64. Barlat, F.; Glazov, M.V.; Brem, J.C.; Lege, D.J. A simple model for dislocation behavior, strain and strain rate hardening evolution in deforming aluminum alloys. *Int. J. Plast.* **2002**, *18*, 919–939. [CrossRef]
65. Cai, S.L.; Li, D.Q.; Liu, S.C.; Cheng, Y.F.; Li, J.H.; Koch, C.C. Multiple gradient structures driving higher tensile strength and good capacity to absorbed energy in aluminum wire processed by cryogenic pre-torsion. *Scr. Mater.* **2022**, *210*, 114436. [CrossRef]
66. Fan, H.; Wang, Q.; El-Awady, J.A.; Raabe, D.; Zaiser, M. Strain rate dependency of dislocation plasticity. *Nat. Commun.* **2021**, *12*, 1845. [CrossRef] [PubMed]
67. Kumar, M.; Mishra, S. Implications of the micromechanical Taylor Factor on work hardening parameters: New perspectives from FFT simulations in DAMASK. *Comput. Mater. Sci.* **2024**, *237*, 112892. [CrossRef]
68. Sarkar, A.; Sanyal, S.; Bandyopadhyay, T.K.; Mandal, S. Implications of microstructure, Taylor factor distribution and texture on tensile properties in a Ti-added Fe-Mn-Al-Si-C steel. *Mater. Sci. Eng. A* **2019**, *767*, 138402. [CrossRef]
69. Hansen, N.; Huang, X. Microstructure and flow stress of polycrystals and single crystals. *Acta Mater.* **1998**, *46*, 1827–1836. [CrossRef]
70. Uenishi, A.; Teodosiu, C.; Nesterova, E.V. Microstructural evolution at high strain rates in solution-hardened interstitial free steels. *Mater. Sci. Eng. A* **2005**, *400–401*, 499–503. [CrossRef]
71. Zhang, K.; Holmedal, B.; Manik, T.; Saai, A. Assessment of advanced Taylor models, the Taylor factor and yield-surface exponent for FCC metals. *Int. J. Plast.* **2019**, *114*, 144–160. [CrossRef]
72. Rafailov, G.; Caspi, E.N.; Hielscher, R.; Tiferet, E.; Schneck, R.; Vogel, S.C. Visualization of texture components using MTEX. *J. Appl. Crystallogr.* **2020**, *53*, 540–548. [CrossRef]
73. Yu, W.; Xin, M.; Li, Y.; Jiang, T.; Wang, H.; Wang, Z.; Xu, G. Tribological and texture analysis in Twin-roll casting 2060 Al-Li alloy. *Mater. Des.* **2022**, *223*, 111253. [CrossRef]
74. Xia, D.; Chen, X.; Huang, G.; Jiang, B.; Tang, A.; Yang, H.; Gavras, S.; Huang, Y.; Hort, N.; Pan, F. Calculation of Schmid factor in Mg alloys: Influence of stress state. *Scr. Mater.* **2019**, *171*, 31–35. [CrossRef]

Disclaimer/Publisher's Note: The statements, opinions and data contained in all publications are solely those of the individual author(s) and contributor(s) and not of MDPI and/or the editor(s). MDPI and/or the editor(s) disclaim responsibility for any injury to people or property resulting from any ideas, methods, instructions or products referred to in the content.